

Title Goes Here

true true

26 febrero, 2021

Contents

1	Introduction	1
2	Data & Methods	1
2.1	Motivation to use complex EOF	2
3	Results	4
3.1	Description of EOFs	4
3.2	Regressions	4
3.3	Relationship with other variables	7
3.4	Tropical sources	15
3.5	Precipitation	17
4	Conclusions	20
5	Appendix	20
5.1	Naive EOFs	20
5.2	Chosen rotations of the EOFs	20
6	References	20

1 Introduction

2 Data & Methods

Hersbach et al. (2019) and Bell et al. (2020)

The phase of principal components is defined up to an additive constant. For real principal components, this constant can be either 0 or π , corresponding to a change in sign. For complex principal components, it can be any number between 0 and 2π (Horel, 1984). In this paper we chose the phase of each of the two complex principal components so that the real and imaginary part are easier to interpret. For the first complex principal component, the phase was chosen so that the time series corresponding to the imaginary part had a time mean of zero.

For the second complex principal component, the phase was chosen so that the coefficient of determination between the Oceanic Niño Index (Bamston et al., 1997) and the real part was minimised. It's important to reassure the reader that this procedure does not create a spurious correlation, it only takes whatever relationship that already exist and aligns it with a specific phase. If the relationship is very weak, the rotation cannot generate a strong relationship.

Table 1: R^2 between pairs of EOFs of each level rounded to two decimals.

200 hPa	50 hPa			
	EOF1	EOF2	EOF3	EOF4
EOF1	0.31	0.02	0.03	0.00
EOF2	0.00	0.02	0.74	0.01
EOF3	0.00	0.04	0.02	0.56
EOF4	0.08	0.06	0.01	0.16

We calculated the PSA1 and PSA2 modes as the third and fourth leading EOF of seasonal mean 500 hPa geopotential height with all seasons together following Mo and Paegle (2001).

ERA5, ERA5 BE,

No mostrar los EOFs no complejos. No tiene sentido mostrarlos si no se analizan.

Relacionar 50hPa con vórtice polar? Temperatura también suma. En 50 el negativo es más intenso que el negativo. ¿Por qué?

Ver qué pasa con U con el EOF1.

En 200 no se ve la señal de jet de la temperatura ¿qué pasa más abajo? en 700 la anomalía de temp coincide más o menos con el geopotential

Mostrar EOF espaciales.

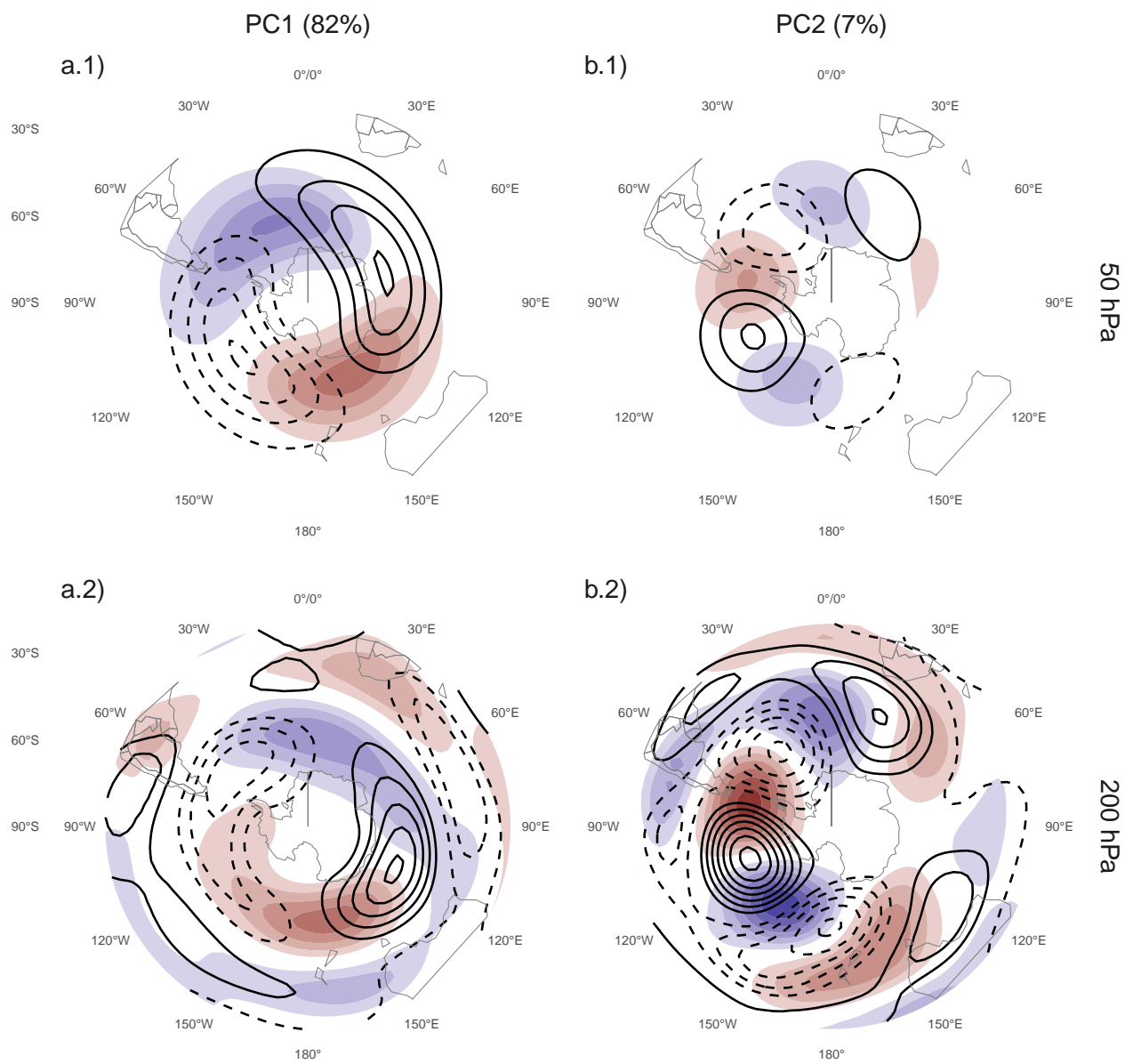
Pp, ¿cuál es la regresión con SAM así en 200 hPa?

2.1 Motivation to use complex EOF

Figure 20a show the spatial pattern of the 4 leading EOF of zonal anomalies of geopotential height for 50 hPa and 200 hPa computed separately. The percentages XXX. At 50 hPa, EOF1 and EOF2 on one hand, and EOF3 and EOF4 on the other are clearly pairs of zonal waves with wave numbers 1 and 2-3 respectively shifted by 1/4 wavelength. That is, each group of two EOFs represents the same zonal wave structure that changes in magnitude and location. Similarly, at 200 hPa EOF2 and EOF3 represent the same zonal wave structure with wave number ~3.

Furthermore, the wave 1 pattern represented by the first two EOFs at 50 hPa is similar to the wave 1 pattern shown as the leading EOF at 200 hPa, and the wave 2-3 pattern represented by the third and fourth EOF at 50 hPa is similar to the wave 3 pattern present in EOF2 and EOF3 at 200 hPa. These similarities suggest some level of joint variability across levels. Figure 20b shows the coefficient of determination between temporal series of each EOF at each level. EOF3 and EOF4 at 50 hPa are highly correlated with EOF2 and EOF3 at 200 hPa. Not only each pair of EOFs represent a single structure within each level, but they represent a coherent pattern of variability between levels. Similarly, the leading EOF of each level are relatively highly correlated, again suggesting an unique mode of joint variability.

Both observations motivate the decision of performing complex EOF jointly between levels. The computation of the EOFs was carried out using data from both levels at the same time, therefore, each complex EOF has a spatial part that depends on longitude, latitude and level, and a temporal part that depends only on time.



(a) Spatial patterns. Real part in shading, imaginary part in contours.

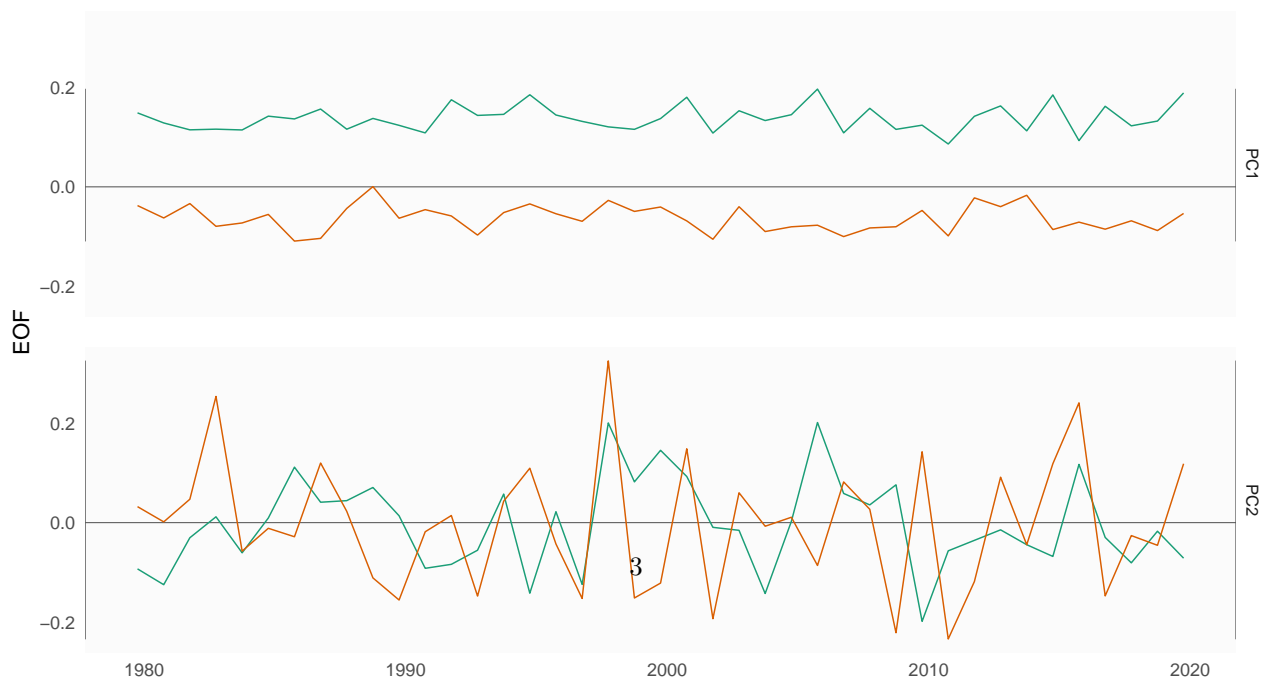


Table 2: R^2 of the absolute magnitude of complex EOFs between 200 hPa and 50 hPa computing EOF separately for each level. The high correlation between levels for the two leading EOFs justifies treating the pattern as a mode of covariability between the stratosphere and the troposphere and, thus, computing the EOFs using both levels at the same time.

200 hPa	50 hPa		
	PC1	PC2	PC3
PC1	0.28	0.02	0.02
PC2	0.00	0.60	0.02
PC3	0.00	0.00	0.01

3 Results

3.1 Description of EOFs

Figures 1a and 1b show, respectively, the spatial and temporal parts of the first two leading complex EOFs of zonal anomalies of geopotential height at 50 hPa and 200 hPa. In the spatial patterns in Figure 1a, the real (in shading) and the imaginary parts (in contour) are in quadrature by construction, so that each EOF describe a single wave-like pattern whose amplitude and position (i.e. phase) is controlled by the magnitude and phase of the complex temporal EOF.

The wave patterns described by these complex EOFs match the patterns seen in the naive EOFs of Figure @ref(fig: cor-eof-naive-1): The first is a wave 1, while the second is a wave 3. Note that in Figure 1b, both parts of the EOF1 have non zero mean. This is due to the fact that the geopotential fields that enter into the algorithm are anomalies with respect to the zonal mean (shown in Figure ??), not the time mean. The variability associated with the first EOF is variability that projects onto the mean zonally anomalous field.

Figure 2 shows temporal series of the two complex EOFs extended beyond the satellite era using the preliminary ERA5 back extension going back to 1950 (which we call the “hybrid ERA5” reanalysis). There is a downward trend in the real part of EOF1 in the hybrid reanalysis (Figure 2a.1, p-value = 0.0011). There is no significant trend in any of the complex parts of EOF2.

3.2 Regressions

The spatial patterns shown in Figure 1a are “pure” EOF patterns. But as they are derived by removing the zonally symmetric circulation, they might not include all the variability that is actually associated with the EOF time series. They are also idealised in that they are forced by construction, to be Hilbert transforms of each other. To get a more realistic view of the real-world variability described by these EOFs, we computed regression patterns of each EOF with the complete geopotential fields.

Figure 3 shows regression patterns of EOF1 and geopotential height. At 50 hPa (Figure 3 row a), both the Real and Imaginary EOF1 are associated with planetary wave 1 patterns, that are 90° off phase. Their phases coincide with the ones shown in Figure 1a.1, with the positive centre of the Real EOF1 located towards the dateline, and the one of the Imaginary EOF1 located over Eastern Antarctica. However, the Real EOF1 pattern is substantially altered by the zonally symmetric circulation. Instead of a clear wave 1 pattern, the regression pattern can be better describes as a monopole with its centre displaced from the South Pole. Similarly affected are the regression patterns at 200 hPa (Figure 3 row b). It is only possible to distinguish some of the wave 1 pattern in relation with the Real EOF1 (Figure @??fig:eof1-regr-gh)b.1). The Imaginary EOF1 shows a much more zonally symmetrical pattern resembling a negative Southern Annular Mode.

With the exception of the Imaginary EOF1, it’s clear that these patterns are very different than the idealised versions shown in Figure 1a, particularly at 200 hPa. Moreover, only in the stratosphere these patterns actually show a distinguishable wave 1 pattern shifted in phase by 90°. This should not be utterly surprising,

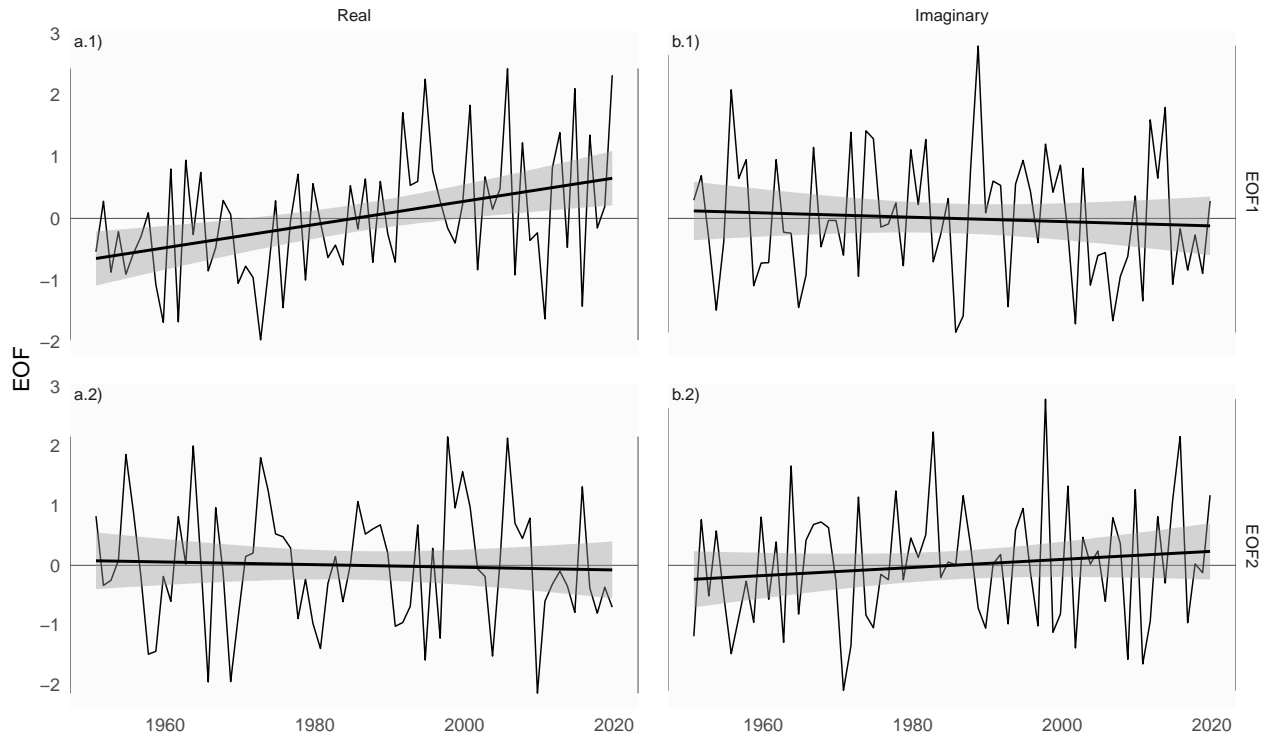


Figure 2: Temporal series extended using ERA5 back extended preliminary edition (period 1950 – 1978) and ERA5 (period 1979 – 2019). Each series is computed by projecting monthly geopotential height zonal anomalies standardised by level south of 20°S onto the corresponding spatial pattern and scaled to zero mean and unit standard deviation.

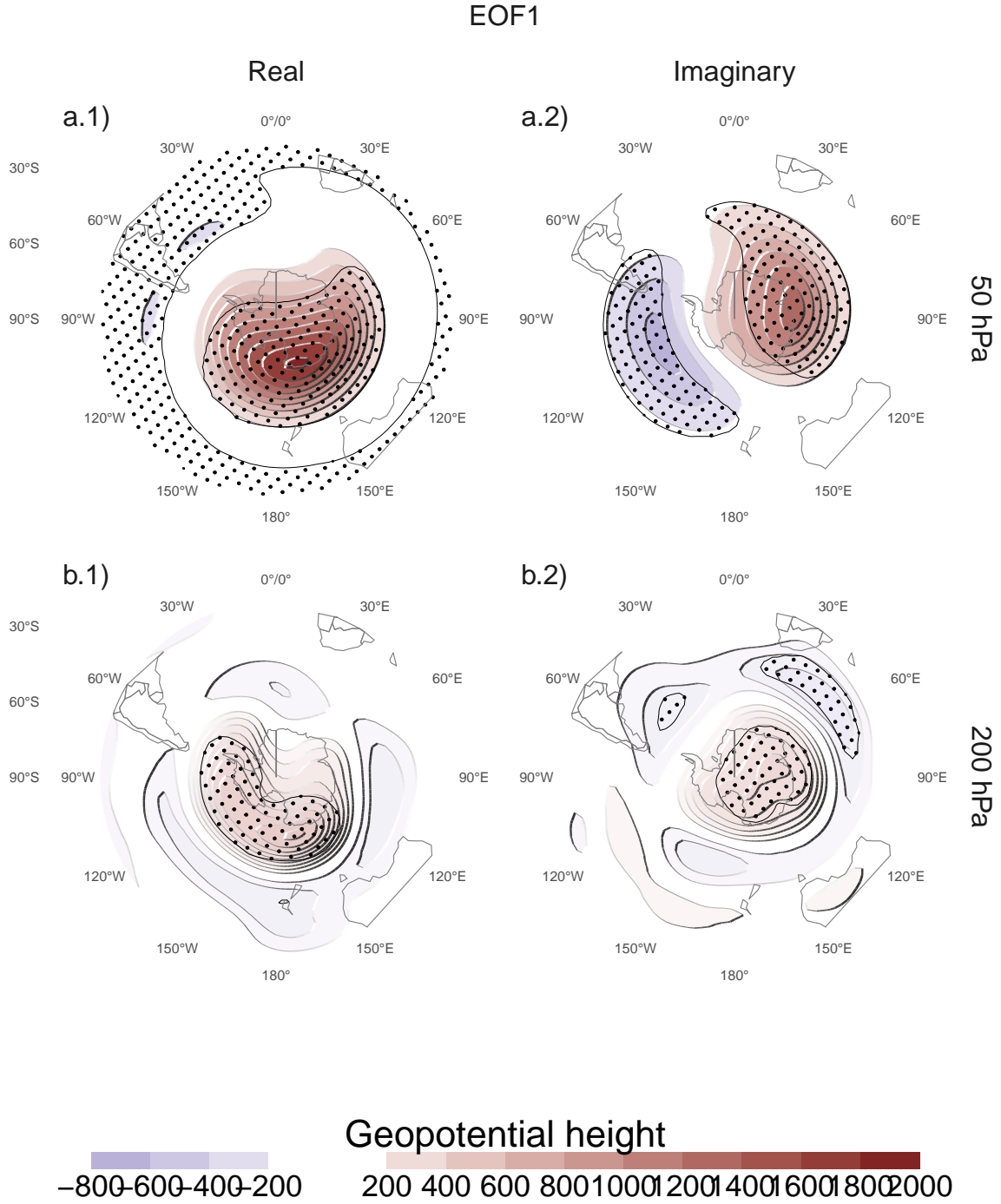


Figure 3: Regression coefficients of the real and imaginary part of the first complex EOF on SON geopotential height for the 1979 – 2019 period. These coefficients come from multiple linear regression involving the real and imaginary part of both EFO2.

since the spatial patterns of the *naive* EOFs only show this feature at 50 hPa, suggesting that using the complex EOF method is “forcing” a wave structure where there is none.

Therefore, the magnitude and phase of the EOF1 are associated with the magnitude and phase of a zonal wave only in the stratosphere. While in the troposphere they are associated with slightly off-centre monopoles.

Figure @ref(fig: eof2-regr-gh) shows the regression pattern of geopotential height and the EOF2. Unlike in the case of EOF1, in this case the regression patterns represent relatively well the *idealised* patterns from Figure 1a. Although there are some differences (particularly in 50 hPa), the wave trains identified before are well characterised and patterns associated with the Real EOF2 are 90° out of phase with those associated with the Imaginary EOF2. Zonal wave 3 dominates all fields, but only in the western hemisphere.

EOF2 then represents a equivalent barotropic wave train that is very similar to the the Pacific South American Patterns (Mo and Paegle, 2001). Comparing the location of the positive anomaly near 90°W in column b of Figure @ref(fig: eof2-regr-gh) with Figure 1 a and b from Mo and Paegle (2001), the Real EOF2 can roughly be identified with the PSA2, while the Imaginary EOF2 resembles PSA1. This separation is not completely meaningful in this case, since by treating this pattern as a single wave train any one pair of orthogonal waves can characterise this variability.

3.3 Relationship with other variables

3.3.1 Ozone

Figure 5 shows regression patterns of EOF1 with air temperature. In both levels, the distribution of temperature anomalies mirror the geopotential height anomalies in 50 hPa. To understand the vertical distribution of these anomalies, Figure @??fig:t-vertical)) shows the regression pattern of EOF1 and zonal anomalies of air temperature averaged between 80°S and 35°S. Both pars of EOF1 are associated with a temperature wave 1 pattern which changes phase around 10 hPa. This switch in the sign of the correlation in temperature at 10 hPa suggest a relationship with Ozone, since its indicative of the effects of planetary waves in the advection of Ozone (Hartmann and Garcia, 1979; Rood and Douglass, 1985; Smith, 1995).

To confirm this possibility, Figure 7 shows regression maps of EOF1 with fields of Total Ozone Column (TOC). It shows zonal wave 1 pattens in TOC associated with both phases of EOF1. Climatologically, the springtime Ozone minimum is located off the South Pole and towards the Weddell Sea (Wirth, 1993). Thus, the Real EOF1 regression pattern (Figure 7a) coincides with the climatological position of the ozone whole while the one for the Imaginary EOF1 is shifted by 90°. This suggest that the EOF1 can be a complete description of the TOC zonal wave 1.

Indeed, Figure 7 shows the relationship between amplitude and phase of the planetary wave 1 in Total Ozone Column between 70°S and 45°S and amplitude and phase of the EOF1. The correlation between the zonal wave 1 of ozone and EOF1 (computed as the mean cosine of the difference in phase) is 0.87 (CI: 0.77 – 0.93). As expected from the location of anomalies in Figure @ref(fig: o3-regr), the Real EOF1 drives the relationship with amplitude and the Imaginary EOF1 drives the relationship with phase (not shown).

3.3.2 PSA

We will show that the EOF2 offers an alternative way of representing the PSA which has several advantages over using the second and third principal components .

Figure @??fig:psa-eof2) shows the relationship between the two PSA indices and the Real and Imaginary phase of EOF2. As anticipated by Figure @??fig: eof2-regr-gh), there is a strong correlation between PSA1 and Imaginary EOF2 (Figure @??fig:psa-eof2)b.1), and between PSA2 and Real EOF2 (Figure @??fig:psa-eof2)a.2). Conversely, there is no relationship between PSA1 and Real EOF2, and between PSA2 and Imaginary EOF2 (Figure @??fig:psa-eof2) panels a.1 and b.2). So not only this EOF2 represents well both

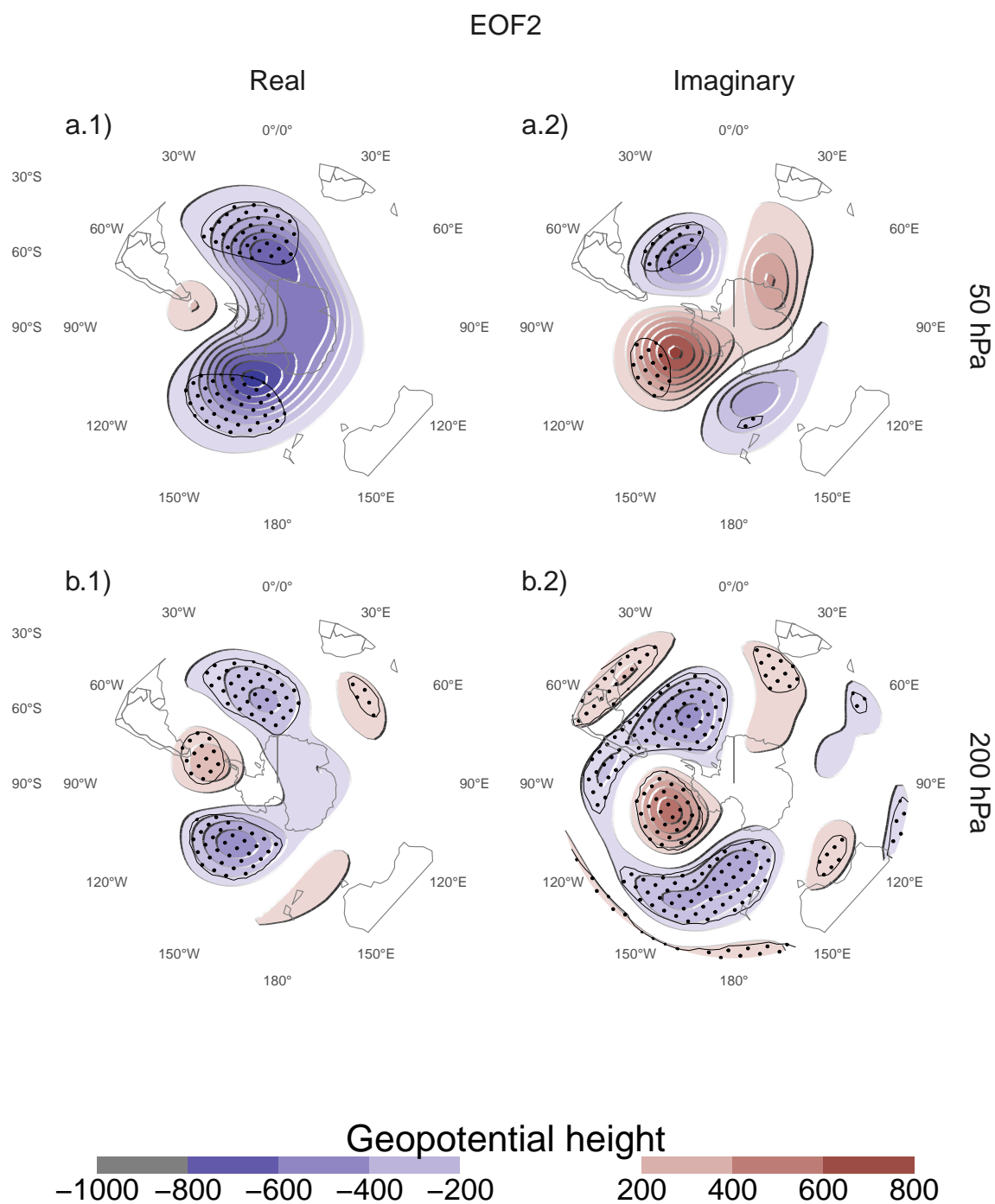


Figure 4: Same as Figure 3 but for the second EOF.

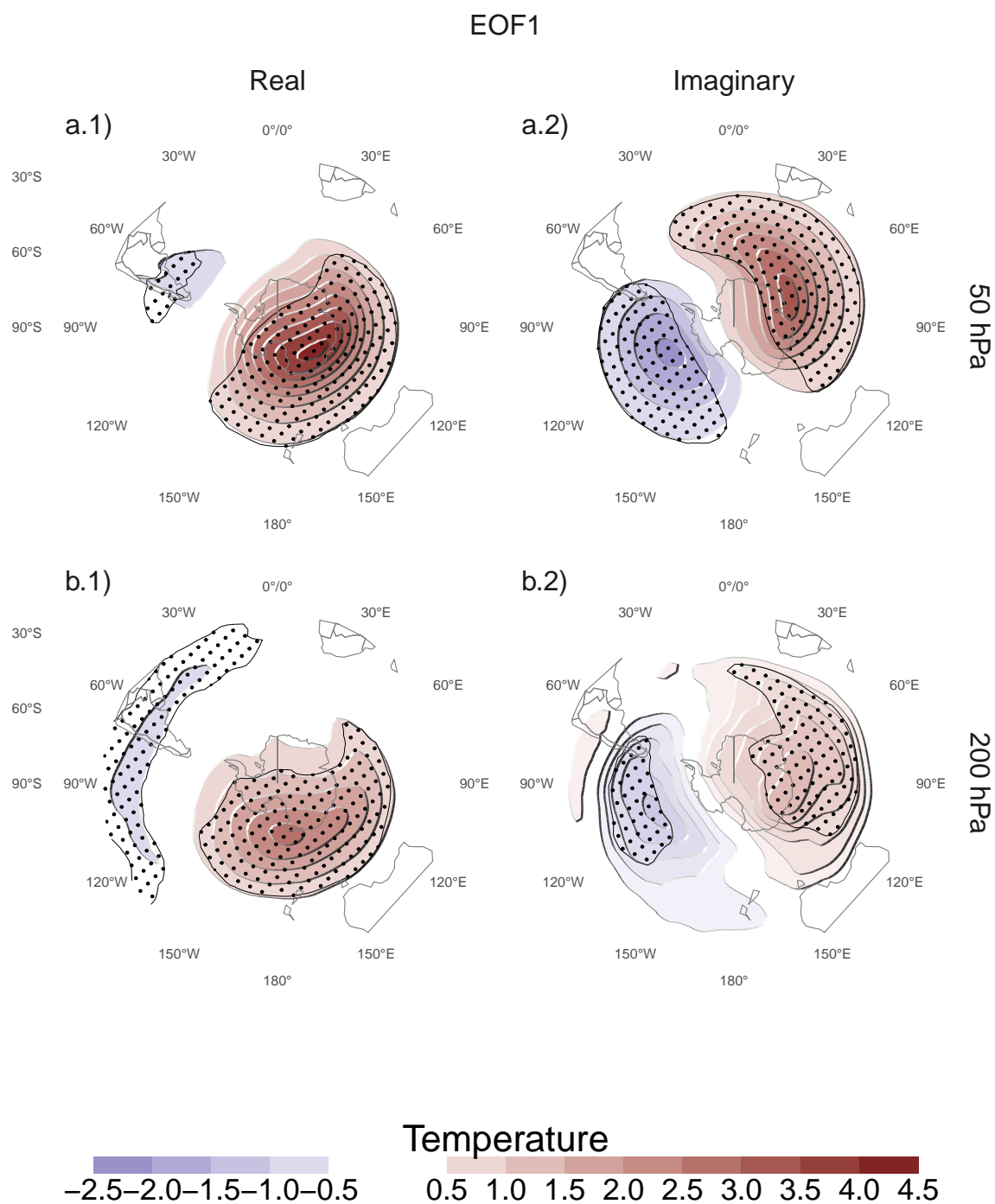


Figure 5: Same as Figure 3 but for air temperature.

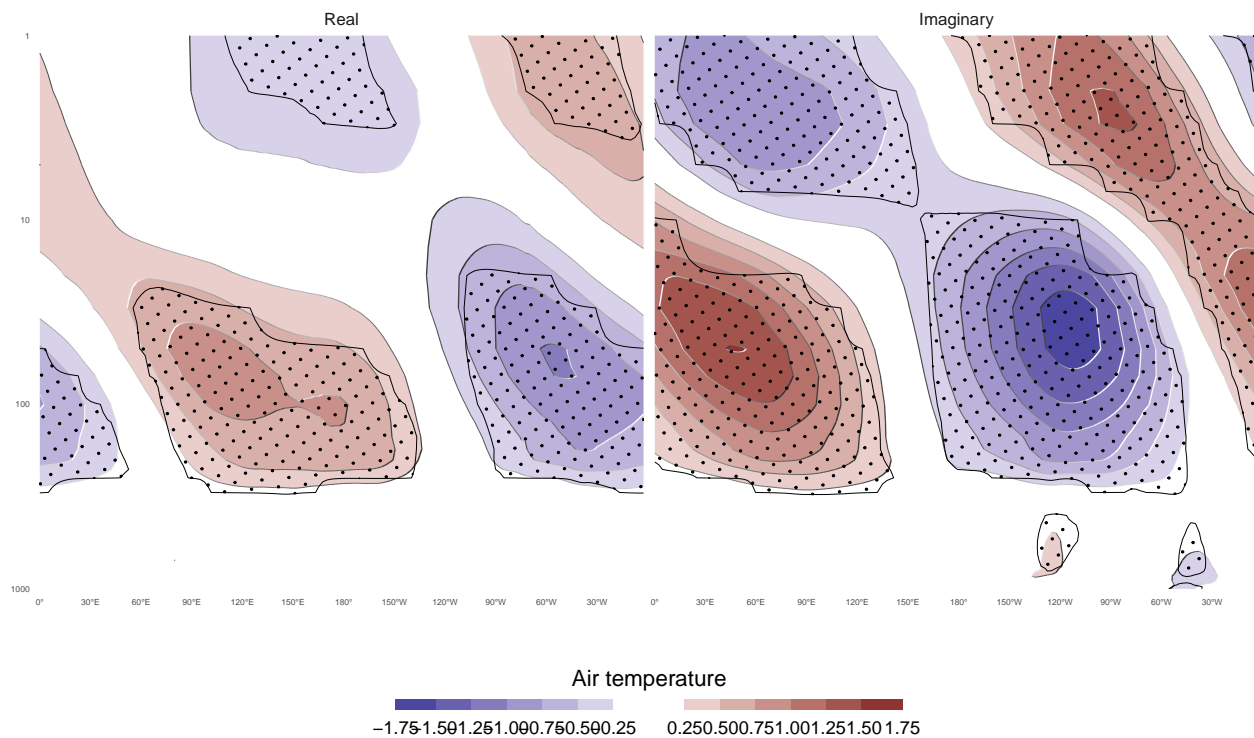


Figure 6: Regression of EOF1 with mean air temperature between 80°S and 25°S.

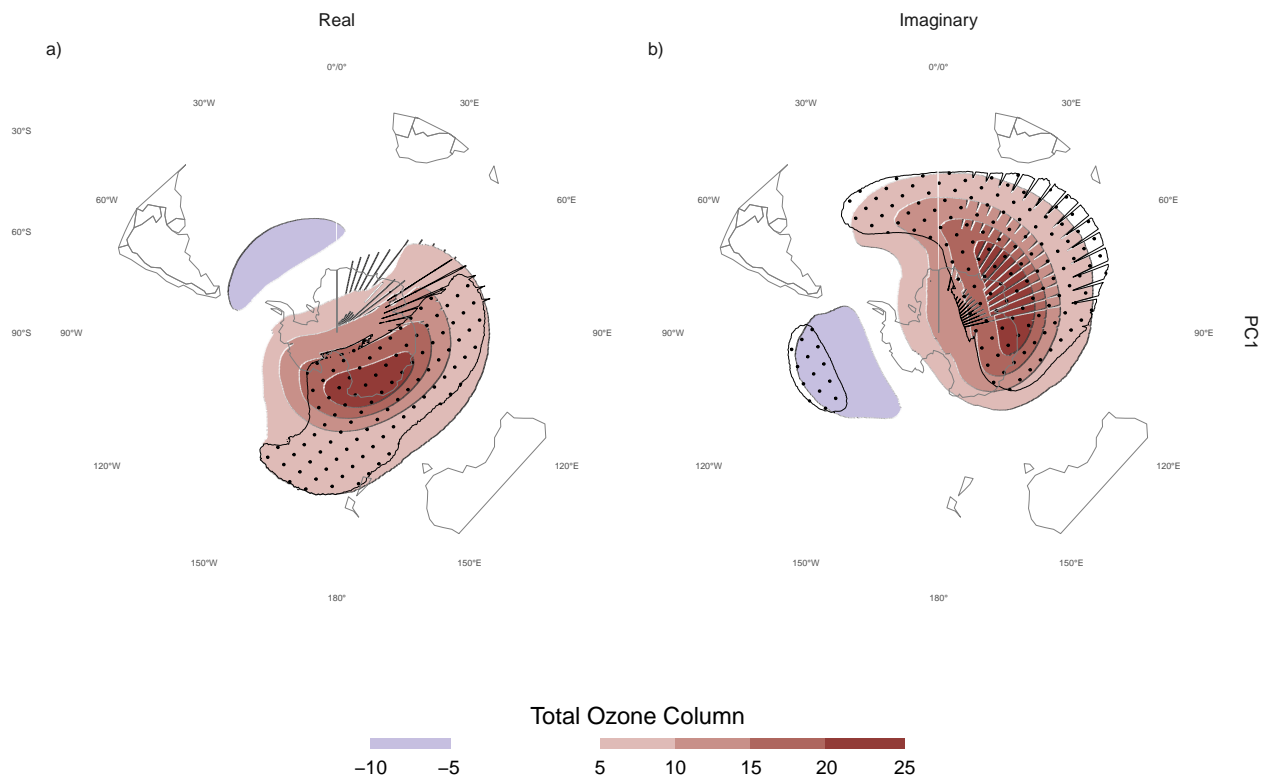


Figure 7: Regression of standardised EOF1 and Total Ozone column.

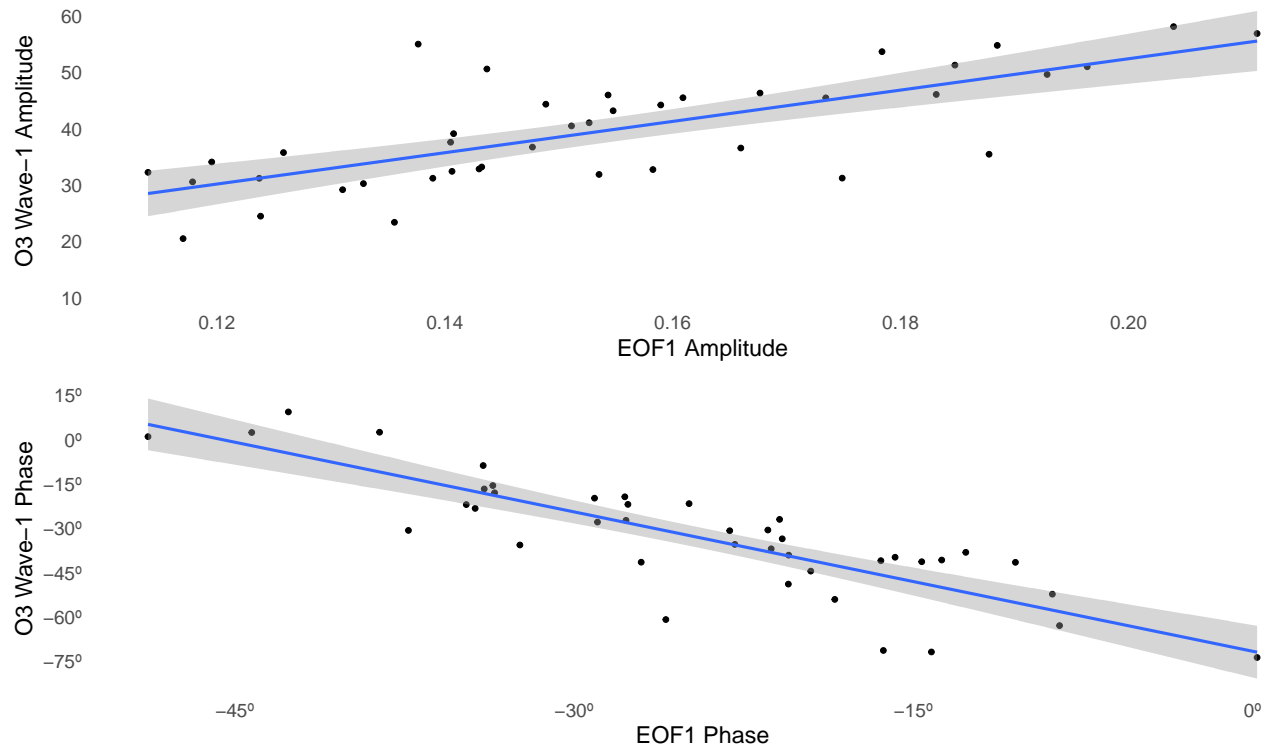


Figure 8: EOF1 and wave1 o3 amplitude.

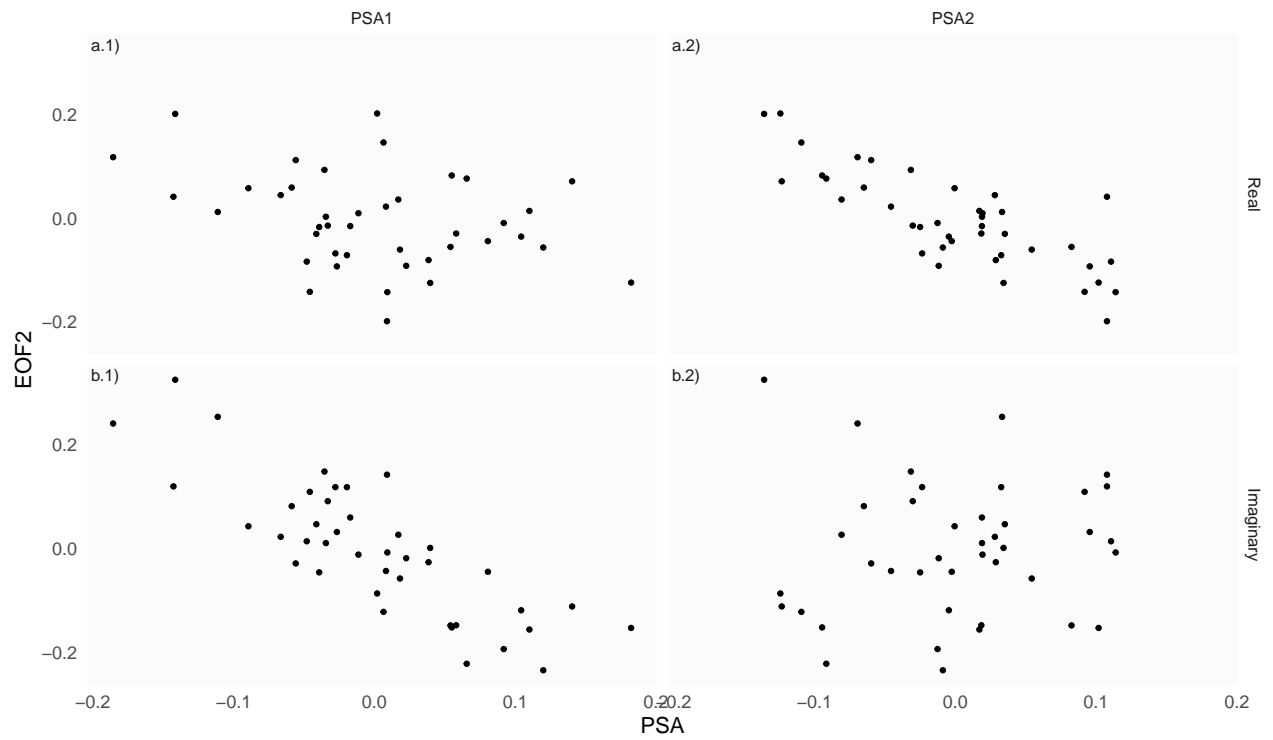


Figure 9: EFO2 and PSA

the spatial structure and temporal evolution of the PSA modes, but it's also possible to make a rather clean association between its two phases and the two PSA modes.

This particular rotation of EOF2 is the one which maximises the relationship between ENSO and Imaginary EOF2. It is also the same that maximises this clean association between EFO2 parts and PSA modes. The reason that the “naive” principal component analysis arrives naturally to this optimal separation is that the imaginary phase is the most common phase (Figure 10), so it naturally appears first when performing a Principal Component Analysis.

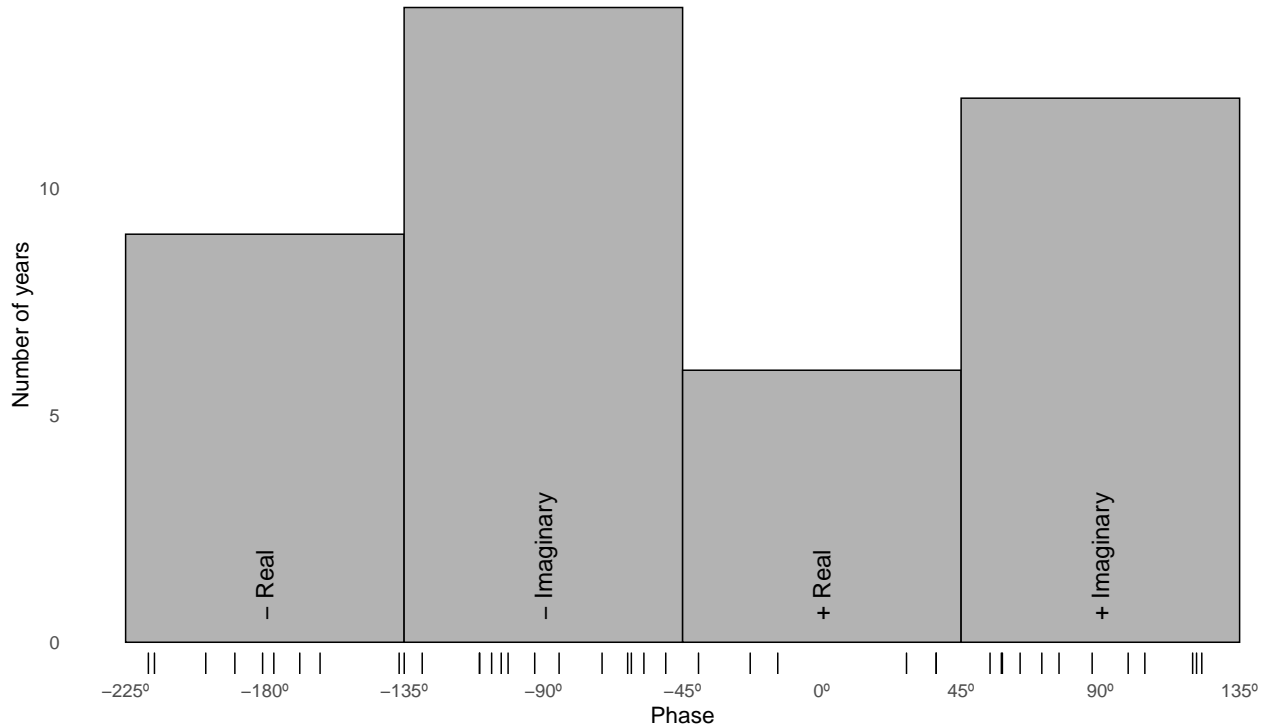


Figure 10: Histogram of phase distributions of EOF2.

By aligning the imaginary phase with the direction with maximum relationship with ENSO, we also aligned it with the phase of maximum occurrence. This is analogous to the method in Irving and Simmonds (2016), who used reprojection and Fourier filtering to detect “PSA-like” variability and defined as the proper PSA using the peaks of the phase distribution (Compare our Figure @ref:(phase-histogram) with their Figure 6).

The advantage of our method is that it is much simpler to implement, it provides magnitude and phase naturally, and it facilitates the description of this mode as a propagating wave instead of as standing oscillation.

3.3.3 SAM

#> [1] 0

Figure 11 shows the coefficient of determination between the EOFs and three SAM indices. The SAM index represents the leading EOF of monthly geopotential height fields south of 20°S at each level. The A-SAM and S-SAM indices represent, respectively, the zonally asymmetric and symmetric component of the SAM and are obtained by projecting the zonally asymmetric and zonally symmetric part of the SAM spatial pattern onto monthly geopotential height fields (Campitelli et al. (2021)). Since the analysis here is only for the SON trimester, monthly values were averaged across semesters (weighted by the number of days in each month).

Both EOFs bear some modest relationship with the SAM index (thick green line in Figure 11), although not statistically significant at every level. The split between A-SAM and S-SAM gives more insight into the

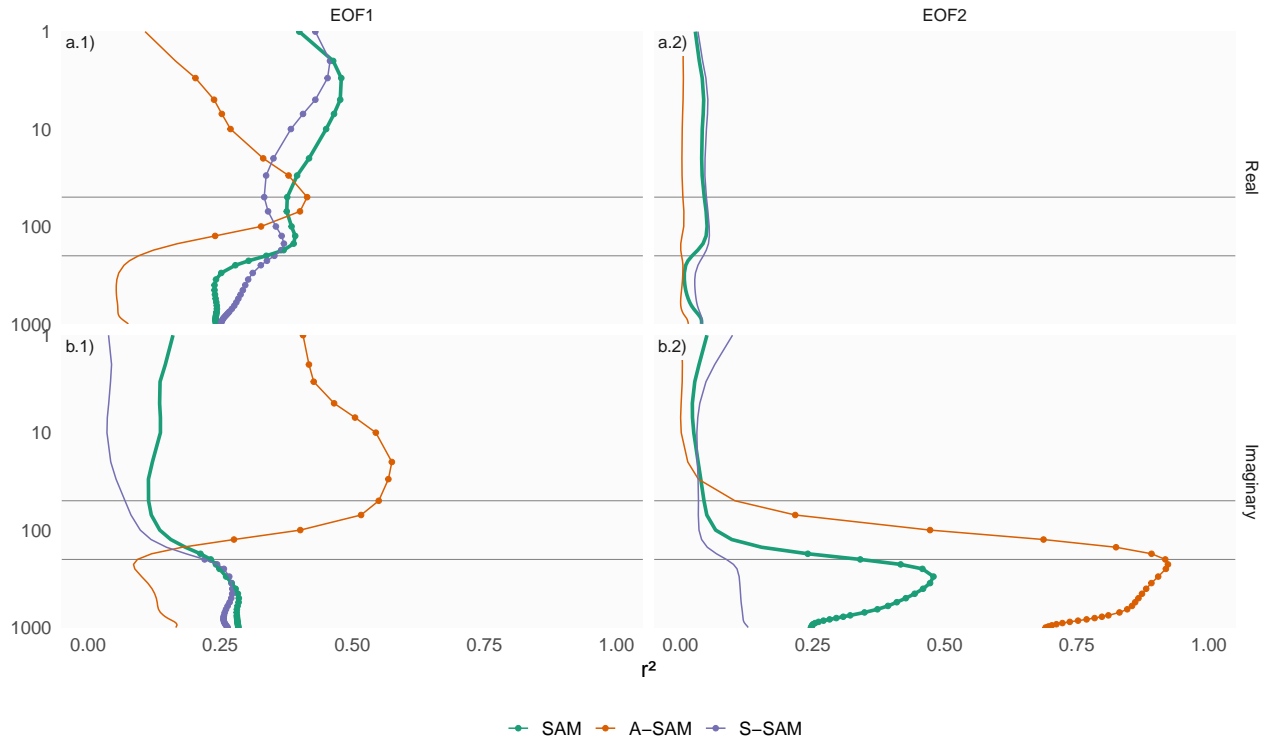


Figure 11: Coefficient of determination between the real and imaginary part of each EOF and the SAM, Asymmetric SAM (A-SAM) and Symmetric SAM (S-SAM) indices computed at each level according to Campitelli et al. (2021). Points mark estimates with p-value < 0.01 corrected for False Detection Rate (Benjamini and Hochberg, 1995).

nature of the relationship. The relationship between the SAM and the imaginary EOF1 (Figure 11.b1) is mediated by S-SAM in the troposphere, but by the A-SAM in the stratosphere.

The Imaginary EOF2 is related with the SAM through the A-SAM in the troposphere, with up to -96% of shared variance, reached at 225 hPa (Figure 11.b2).

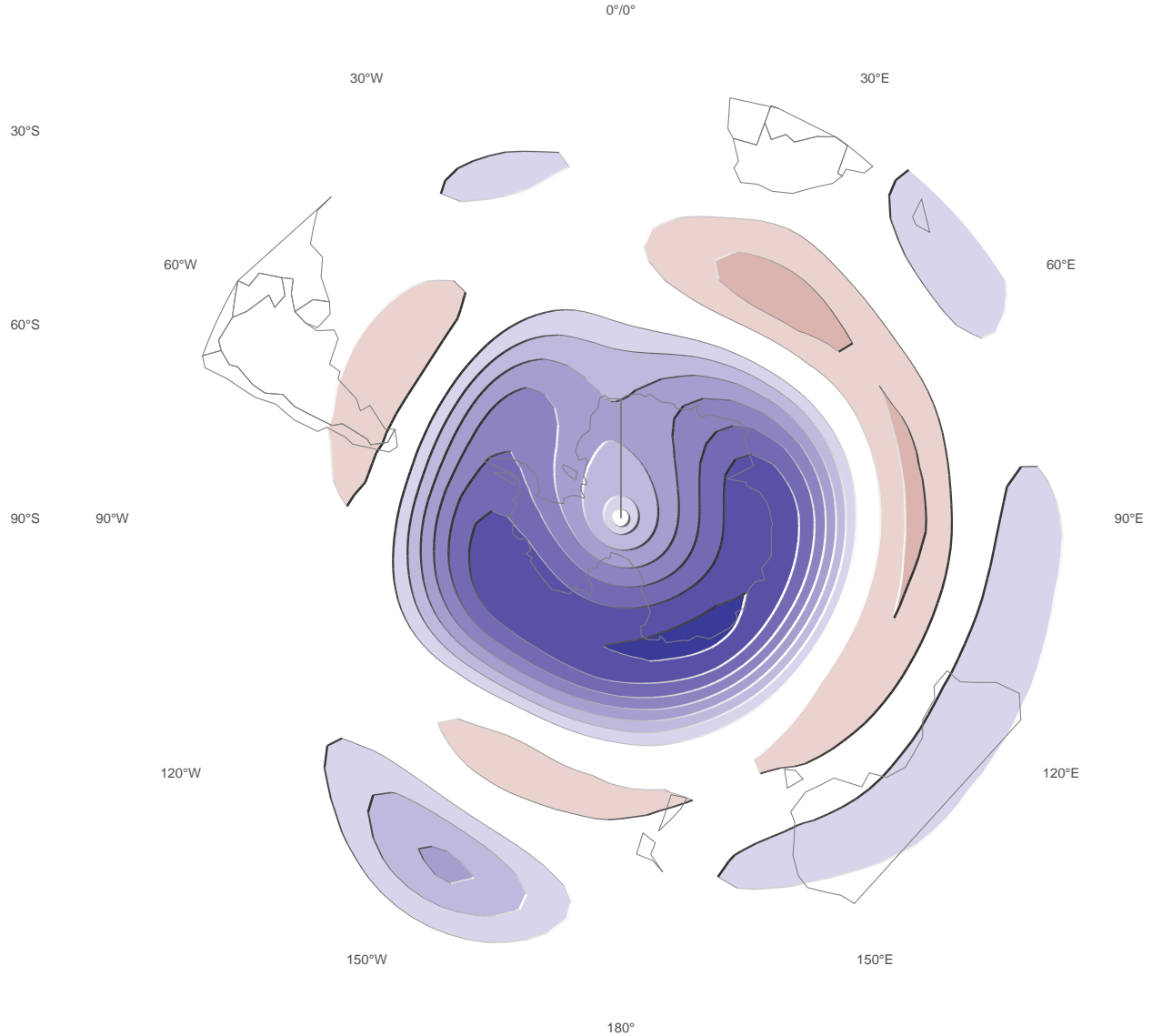


Figure 12: Spatial pattern of the leading EOF of 200 hPa geopotential height with the variability of EOF2 filtered out South of 20°. Arbitrary scale.

As a further illustration, Figure 12 shows the spatial pattern of the leading EOF of 200 hPa geopotential height when the variability associated with EOF2 is removed. The resulting pattern is an nearly zonally symmetrical annular mode. This mode is highly correlated with SAM (0.75 (CI: 0.58 – 0.86)), but only with the symmetrical part (0.88 (CI: 0.79 – 0.94)). Note that the usual definition of the PSA modes as the second and third EOFs creates modes orthogonal to the SAM (defined as the first EOF) and thus impedes this kind of filtering.

This suggests that the asymmetric part of the SAM might be statistical contamination from one phase of the PSA. Figure 13 serves as an illustration of this kind of statistical mixing of independent modes. It shows the leading (and only) EOFs of a synthetic dataset if 41 years created by adding a perfectly zonally symmetrical

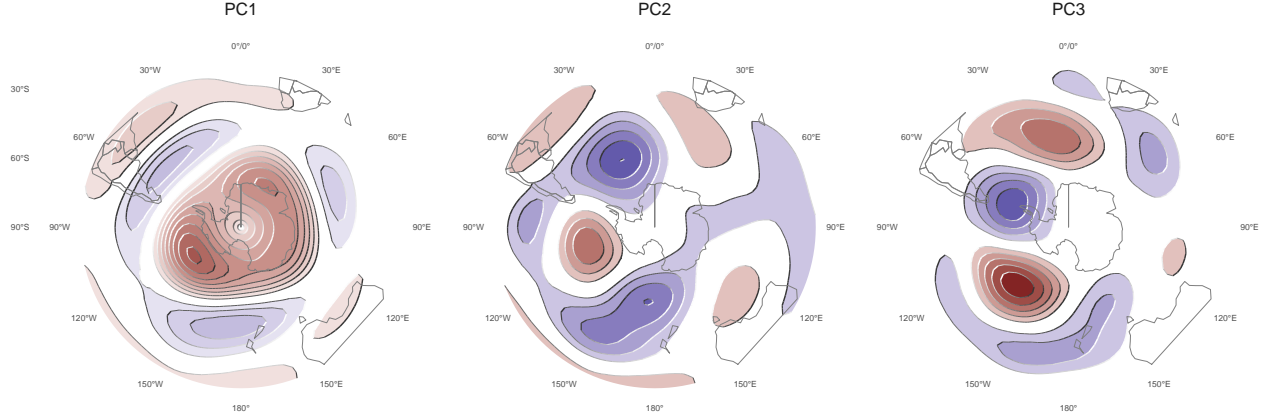


Figure 13: Principal components of a synthetic data set of geopotential height as the sum of the fields predicted by the EOF2 plus perfectly zonally symmetric SAM-like anomalies with random amplitude.

SAM-like pattern with random amplitudes taken from the real SAM, and geopotential height anomalies predicted by EFO2. Even though by construction this dataset has a perfectly symmetric SAM, the EOF decomposition mixes this mode with parts of the the zonally asymmetric EOF2 pattern, resulting in a pattern eerily similar to the real SAM pattern.

This demonstrates that the zonal asymmetries of the SAM could very well be mostly a statistical artifact. Since many surface impacts are mediated by the asymmetric component, as well as the relationship between SAM and ENSO (Campitelli et al., 2021), this potential issue could affect the interpretability of many results involving the SAM. Studies on the relationship between the SAM and the PSA pattern would be particularly difficult to interpret.

3.4 Tropical sources

Figure 14 shows regression maps between EOF2 and Sea Surface Temperatures (SST) Streamfunction at 200 hPa. The Imaginary EOF2 is associated with strong positive SST anomalies on the Central Pacific and negative anomalies on an area across the North of Australia and New Zealand, the South Pacific Convergence Zone (SPCZ) (Figure 14.a2). This pattern is almost canonically positive ENSO and indeed, the correlation between the Imaginary EOF2 and the Oceanic Niño Index ((Bamston et al., 1997)) is very high 0.76 (CI: 0.59 – 0.86). Streamfunction anomalies show a coherent picture. The Imaginary EOF2 is associated with strong wave-like streamfunction anomalies emanating from the tropics (Figure 14.b2). This is consistent with what we know of the effect of ENSO on the extratropics: SST anomalies initiate anomalous convection that excites Rossby waves that propagate meridionally towards higher latitudes.

Since the Real EOF2 represents just a different phase of the same wave train, one would expect that it would show a similar forcing pattern to the Imaginary EOF with a slight translation of its location. However, Figure 14.a1 and b1 show that the Real EOF2 is not associated either with any significant SST nor streamfunction anomalies in the tropics. The correlation between the Real EOF2 and ENSO is also not significant (). This lack of tropical signal suggests a radically different nature of the different phases of the EOF2 wave train.

To better explore the relationship between tropical forcing and phase of the EOF2, Figure 15 plots the ONI index and the phase of the EOF2 for each year between 1979 and 2019, highlighting years in which the magnitude of EOF2 was higher than 50% of the years. In years with positive ENSO, the phase of the EOF2 is always around $+90^\circ$ (corresponding with positive imaginary part) and vice versa. In years with near neutral ENSO, the phase of the EOF2 is much more variable. The black line in Figure 15 tries to quantify this relationship. Is the equation $ONI = 1.1 \sin phase$, whose coefficient we fitted by weighted least squares using the magnitude of the EFO2 as weight. The r^2 corresponding to the fit is 0.56, with p-value < 0.001 .

Figure 15 suggest that strong EOF2 years tend to coincide with strong ENSO years. The correlation between

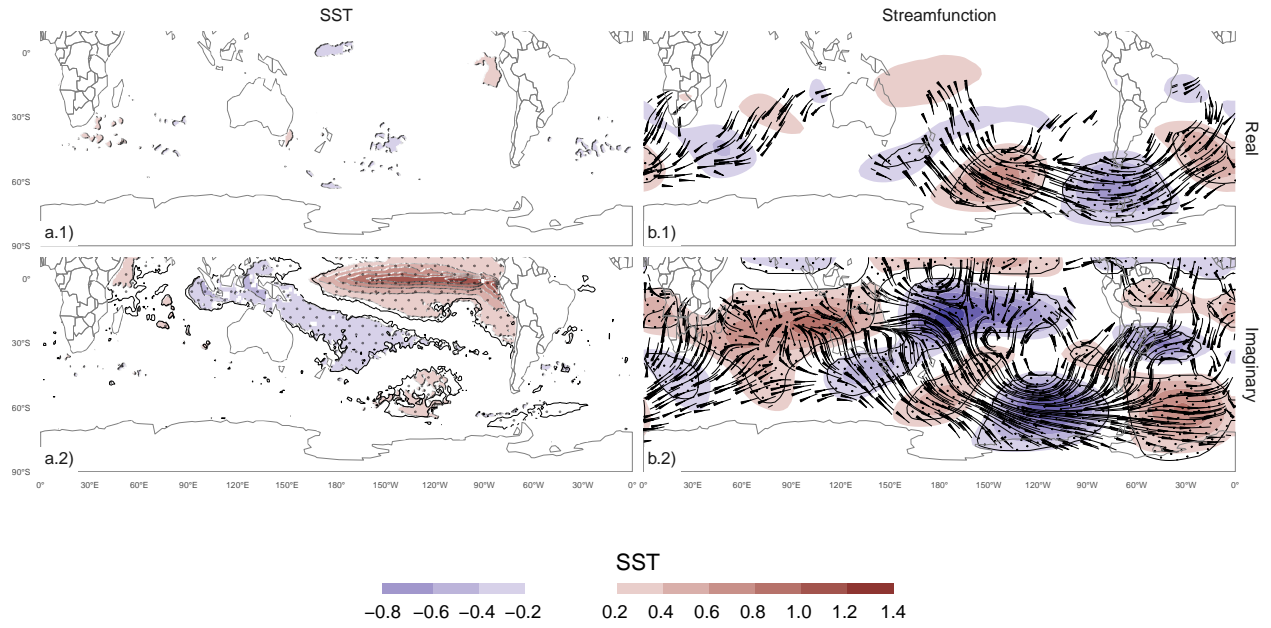


Figure 14: Regression maps of EOF2 with SST (column a) and streamfunction zonal anomalies with their corresponding activity wave flux (column b). Areas marked with dots have p-values smaller than 0.05 adjusted for FDR.

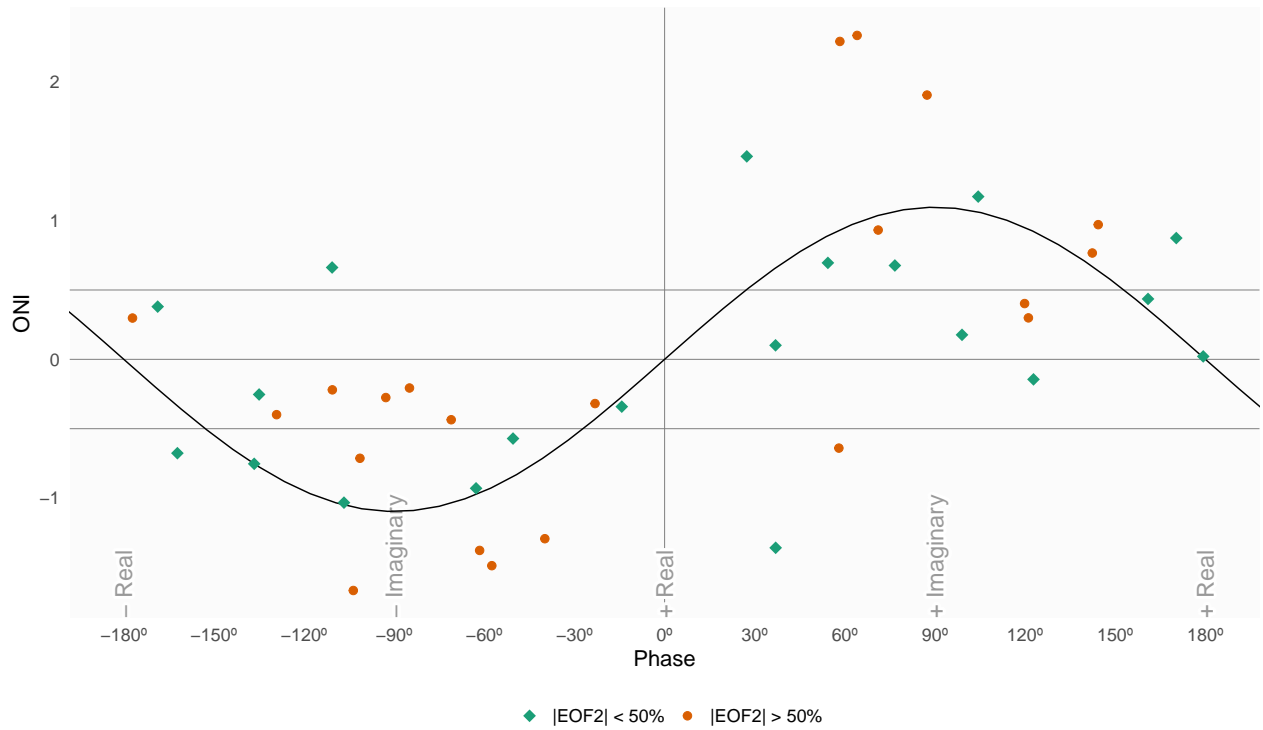


Figure 15: Relationship between ENSO and phase of EOF2 for the period 1979 – 2019. Colours denote years with magnitude of EOF2 greater or smaller than the 50th percentile. Black line is the fit $\text{ONI} \sim \cos(\text{phase}) + \sin(\text{phase})$ computed by OLS weighted by the magnitude of EOF2.

the absolute magnitude of the ONI and the magnitude of the EOF2 is 0.44 (CI: 0.16 – 0.66). This relationship appears to be driven only by the three years with strongest ENSO events in the period (2015, 1997, and 1982) which also coincide with the three years with strongest EOF2 magnitude. If those years are removed, the correlation becomes non-significant (0.044 (CI: -0.28 – 0.36)). Furthermore, the Spearman correlation, which is robust to outliers is also non-significant (0.2, p-value = 0.2). Therefore, the relationship between the magnitude of the EOF2 train wave and ENSO remains uncertain.

All this suggests that the wave train represented by EOF2 can be both forced by tropical SSTs and also a part of the internal variability of the extratropical atmosphere. When internally forced, the wave train has little phase preference. When excited by tropical SST anomalies, it tends to remain locked to the imaginary phase, with the sign of the geopotential anomalies depending on the sign of the tropical SSTs anomalies.

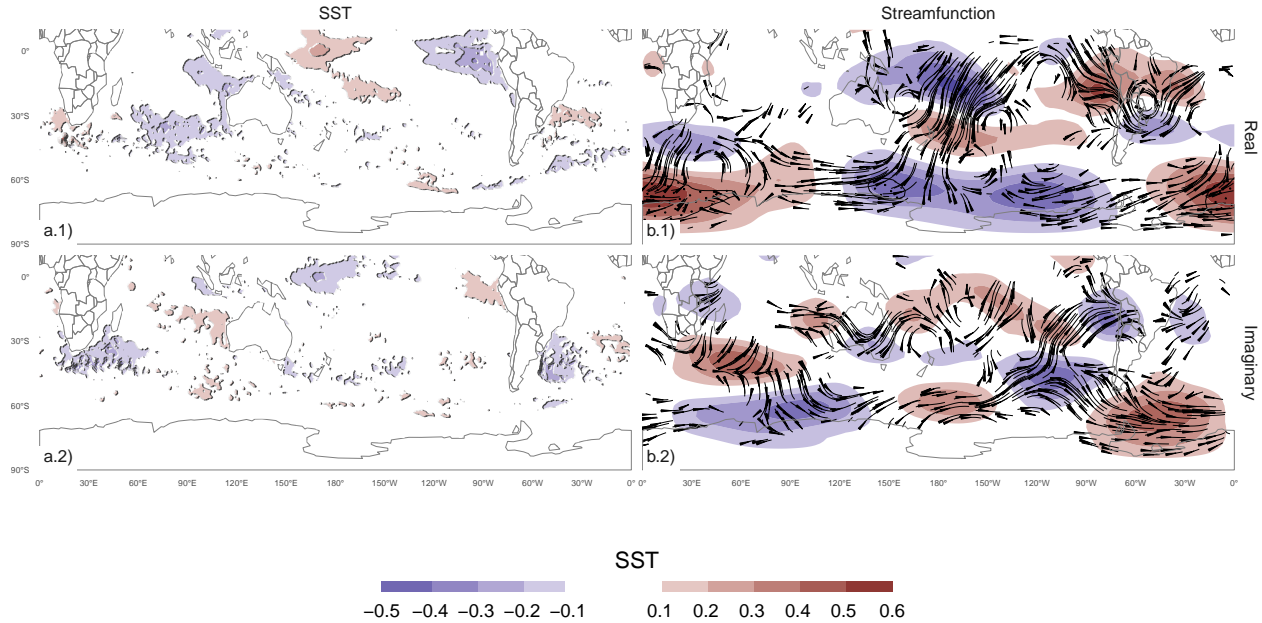


Figure 16: Same as Figure 14 but for EOF1.

Figure 16 shows SST and streamfunction regression maps for EOF1. There is no significant pattern of SST anomalies associated with either the Real or Imaginary EOF1. Consistently, streamfunction anomalies don't show any tropical influence. On the contrary, the Real EOF1 is associated with wave activity fluxes that flow equatorward from the coast of Antarctica around 150°E along with wave activity fluxes that move between the positive and negative of Streamfunction anomalies along Antarctica.

3.5 Precipitation

Figure 17 shows regression maps of seasonal precipitation with each EOF in South America. EOF1 (Figure 17 column a) is associated with increased precipitation over Paraguay and some parts of Brazil. Although these positive anomalies are not very strong. The strongest precipitation anomalies are the ones associated with the Imaginary EOF2. The positive anomalies on Southeaster South America (SESA) and Chile, and negative anomalies over Southern Brazil is a well known springtime precipitation signature of ENSO (Cai et al., 2020) and it's also virtually identical to the precipitation anomalies associated with the Asymmetric SAM (Campitelli et al., 2021). This is not surprising considering the close relationship between the ONI, the Asymmetric SAM index and the Imaginary EOF2 shown previously. The Real EOF2, on the other hand, is associated with negative precipitation anomalies in a smaller area of SESA. The relationship between precipitation anomalies in SESA and the phase of EOF2 follows a curve similar to that of Figure 15 (not shown).

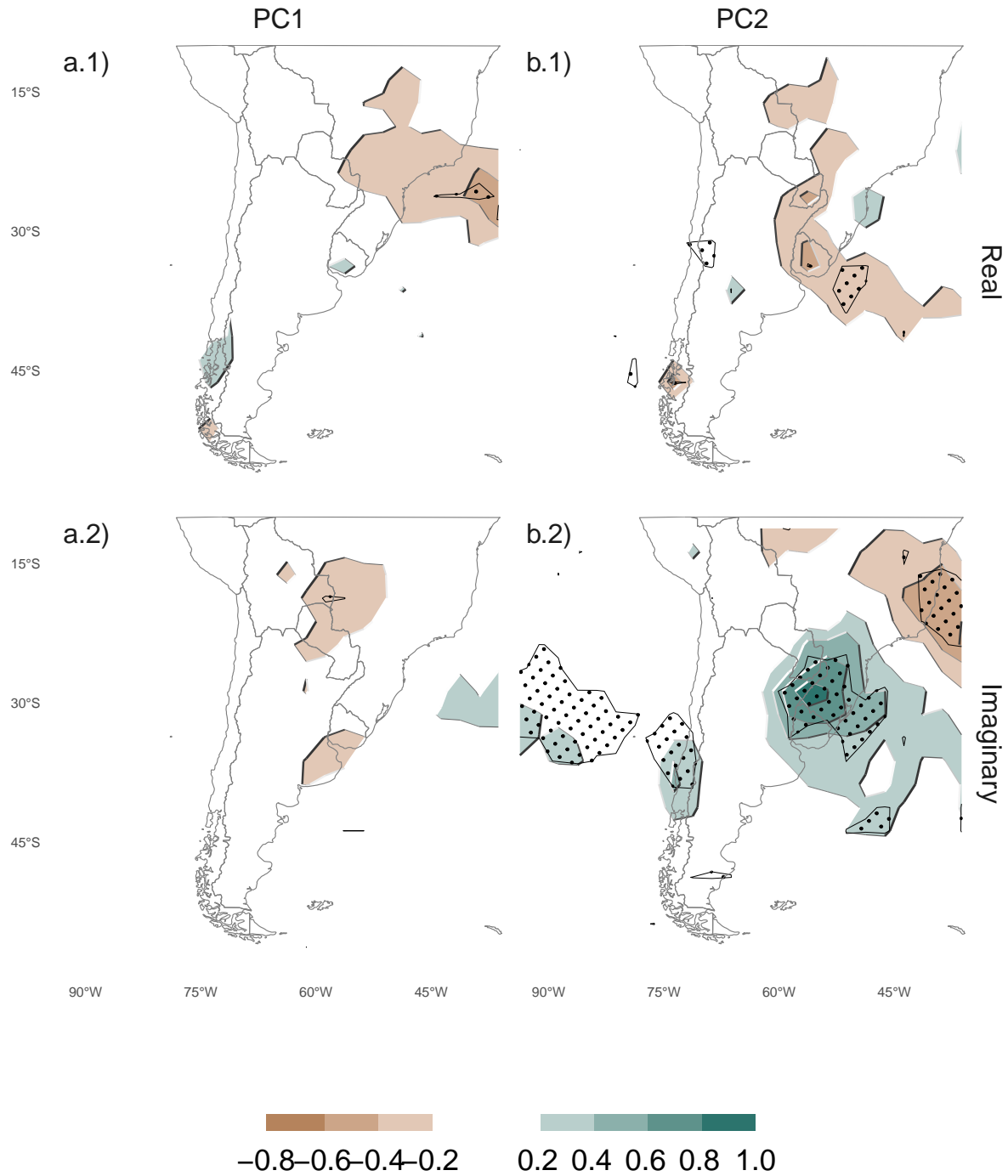


Figure 17: Regression of SON mean precipitation anomalies in South America (mm per day, shaded) and (column a) EOF1 the (row 1) Imaginary and (column 1) Real phase. For the 1979 – 2018 period. Black contours with dots indicate areas with p-value smaller than 0.05 controlling for False Detection Rate.

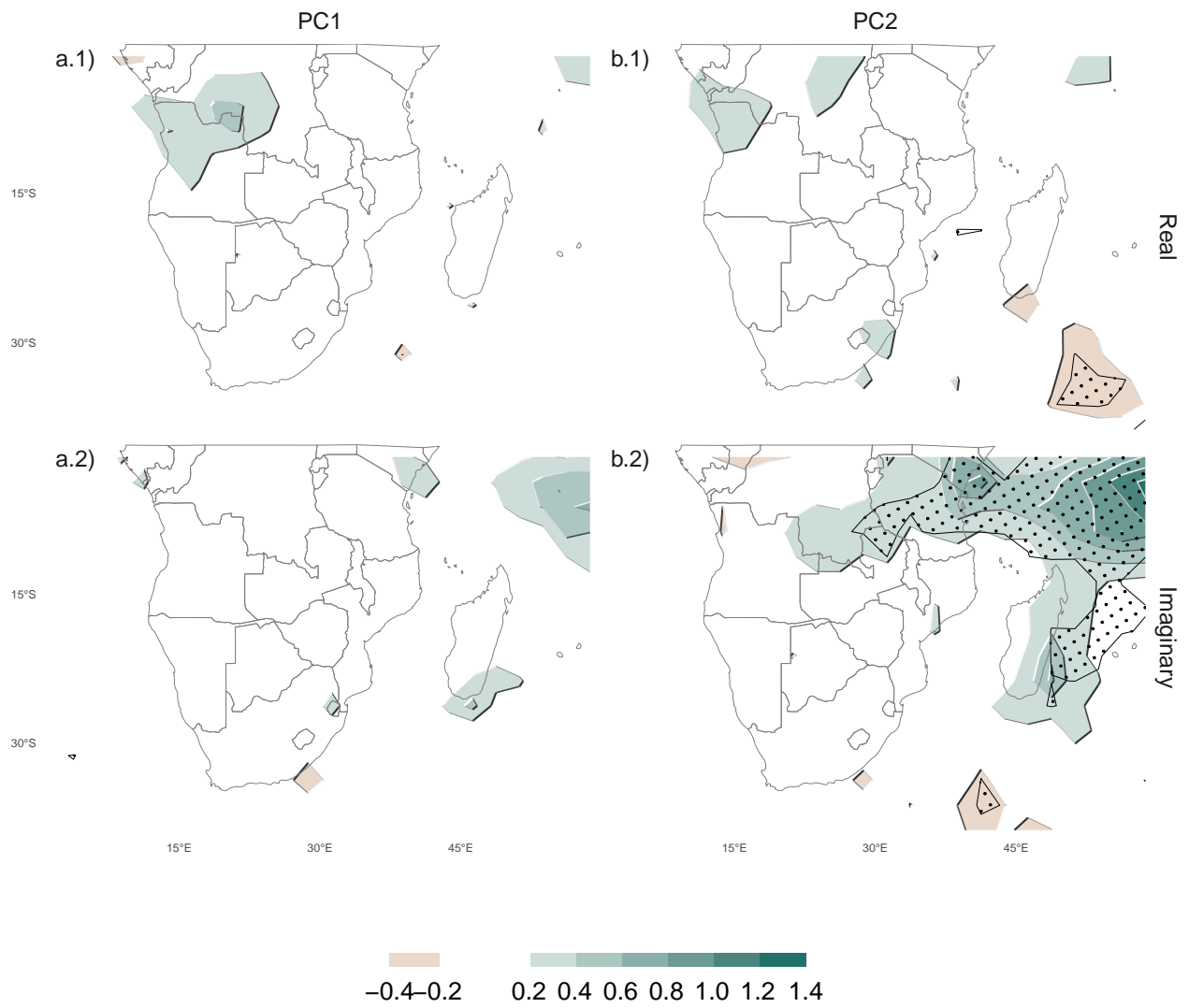


Figure 18: Same as Figure 17 but for South of Africa.

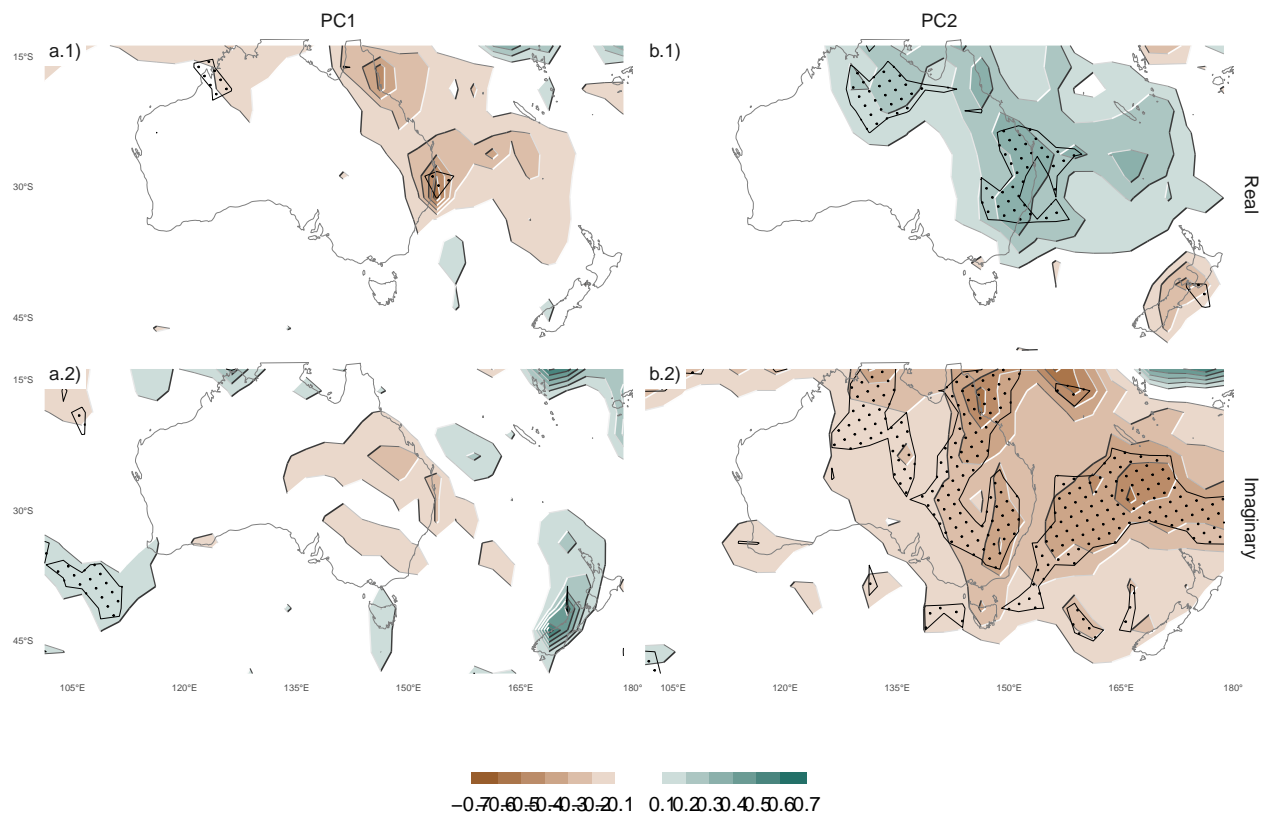


Figure 19: Same as Figure 17 but for New Zealand and neighbouring islands.

4 Conclusions

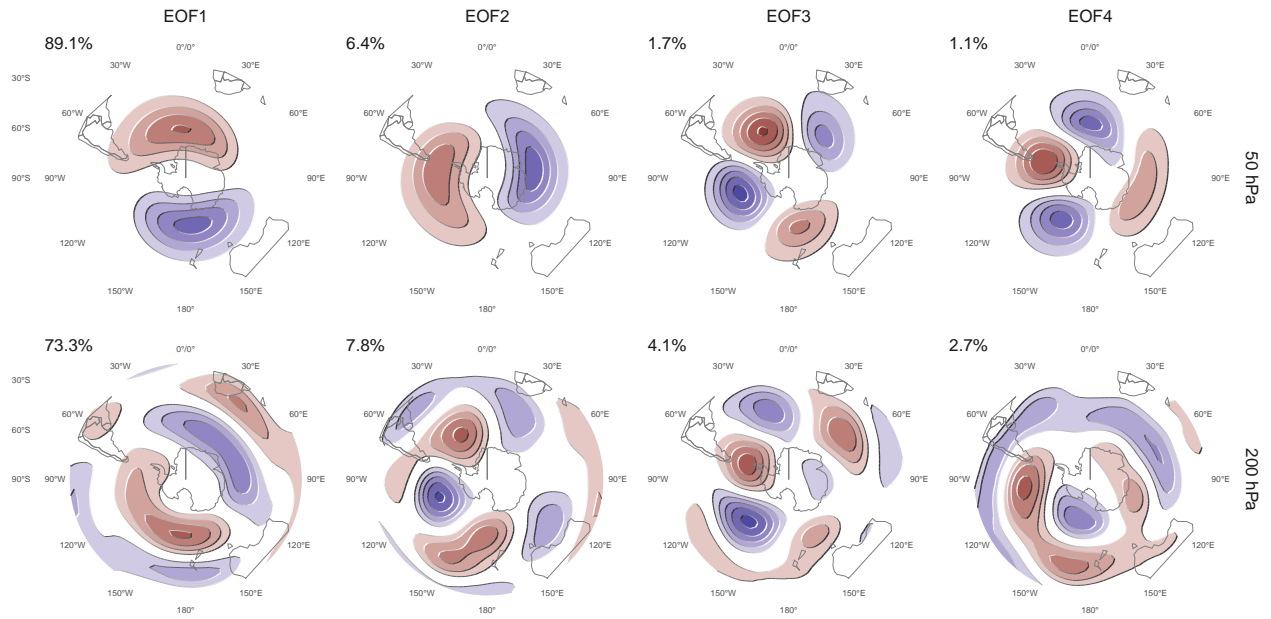
5 Appendix

5.1 Naive EOFs

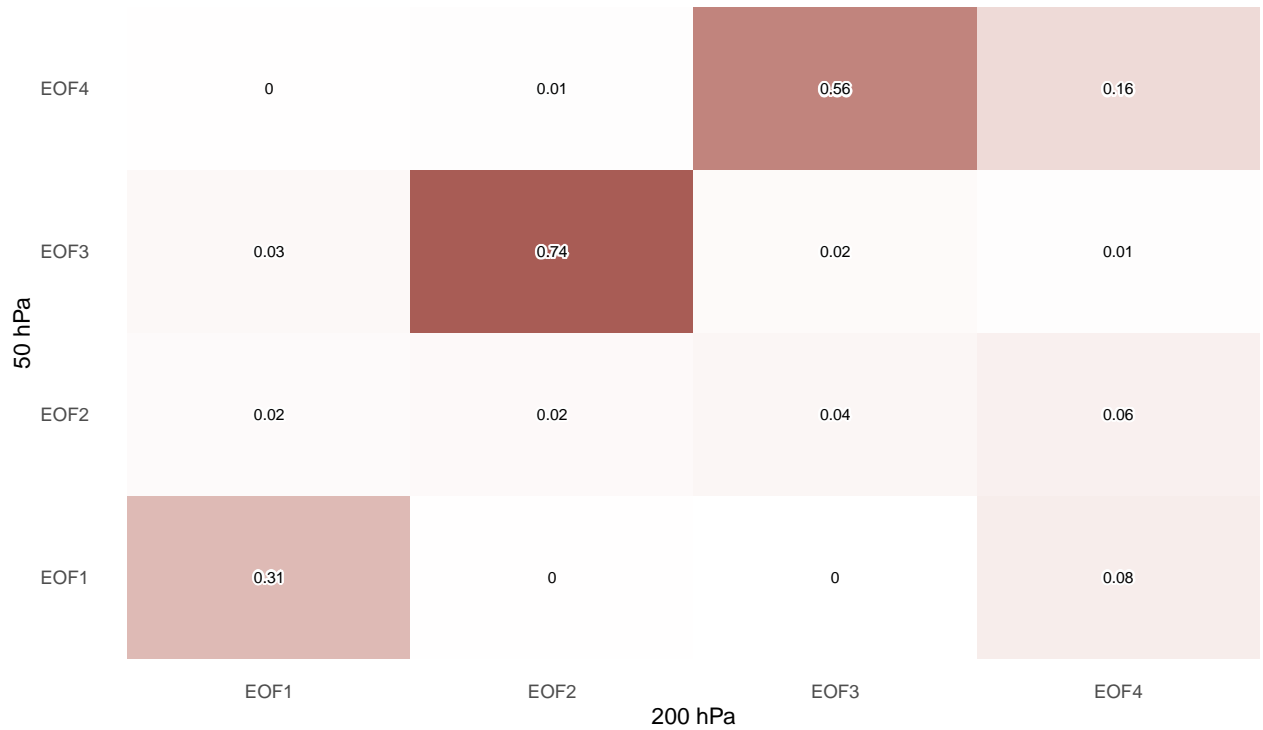
5.2 Chosen rotations of the EOFs

6 References

- Bamston, A.G., Chelliah, M., Goldenberg, S.B., 1997. Documentation of a highly ENSO-related sst region in the equatorial pacific: Research note. *Atmosphere-Ocean* 35, 367–383. <https://doi.org/10.1080/07055900.1997.9649597>
- Bell, B., Hersbach, H., Berrisford, P., Dahlgren, P., Horányi, A., Muñoz Sabater, J., Nicolas, J., Radu, R., Schepers, D., Simmons, A., Soci, C., Thépaut, J.-N., 2020. ERA5 monthly averaged data on pressure levels from 1950 to 1978 (preliminary version). Copernicus Climate Change Service (C3S) Climate Data Store (CDS) (Accessed on <19-02-2021>), <https://cds.climate.copernicus.eu/cdsapp#!/dataset/reanalysis-era5-pressure-levels-monthly-means-preliminary-back-extension?tab=overview>.
- Benjamini, Y., Hochberg, Y., 1995. Controlling the False Discovery Rate: A Practical and Powerful Approach to Multiple Testing. *Journal of the Royal Statistical Society: Series B (Methodological)* 57, 289–300. <https://doi.org/10.1111/j.2517-6161.1995.tb02031.x>



(a) Spatial patterns (arbitrary units). The numbers at the top-left of each panel is the variance explained by each EOF.



(b) Coefficient of determination of the temporal index of each EOF between levels.

Figure 20: Leading 4 EOFs of zonal anomalies of geopotential height at 50 hPa and 200 hPa for the SON trimester and the period 1979 – 2009.

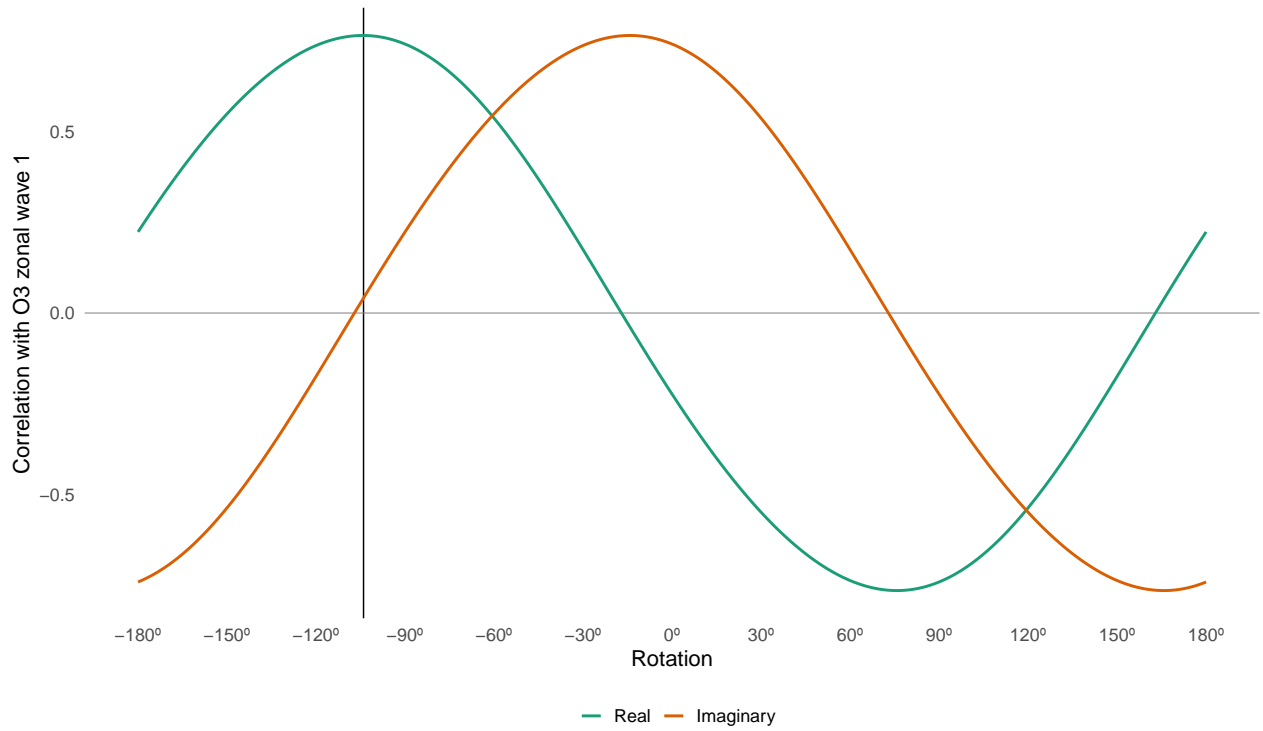


Figure 21: Rotations of PC1

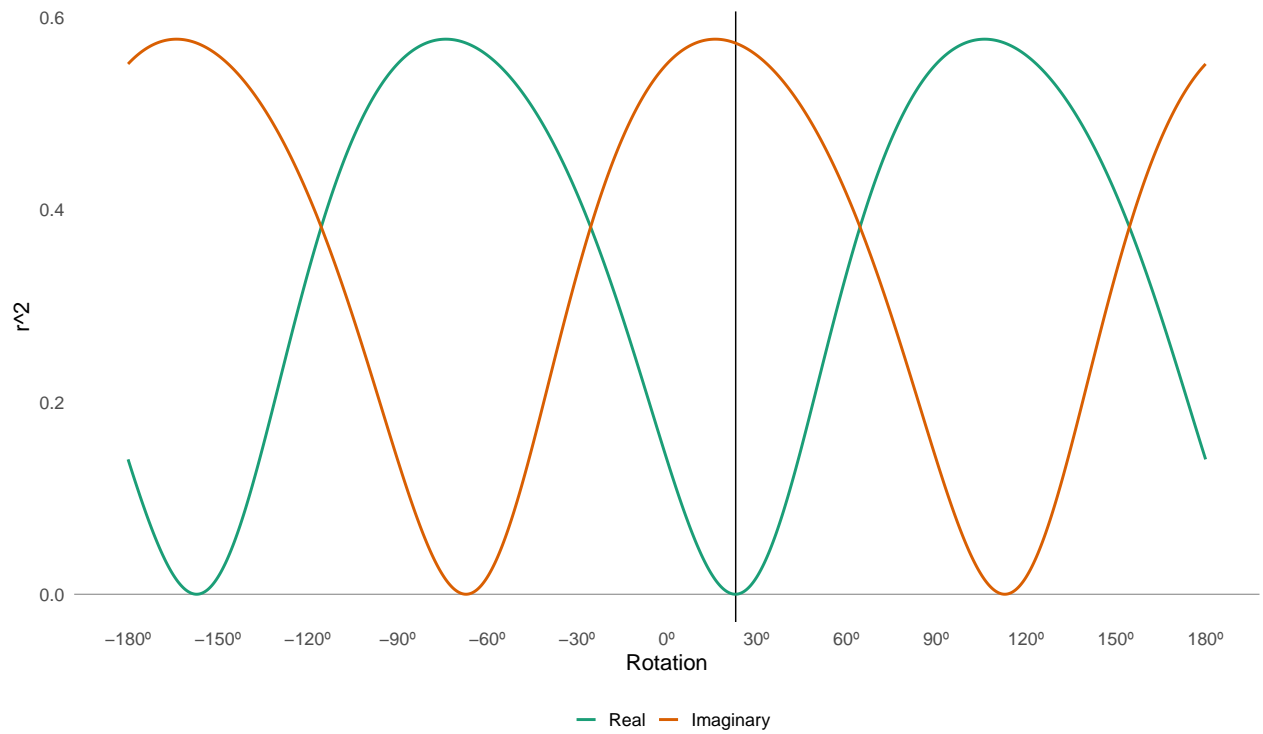


Figure 22: R^2 between EOF2 Real and Imaginary parts and ONI index for different rotation parameters of the real and imaginary parts.

- Cai, W., McPhaden, M.J., Grimm, A.M., Rodrigues, R.R., Taschetto, A.S., Garreaud, R.D., Dewitte, B., Poveda, G., Ham, Y.-G., Santoso, A., Ng, B., Anderson, W., Wang, G., Geng, T., Jo, H.-S., Marengo, J.A., Alves, L.M., Osman, M., Li, S., Wu, L., Karamperidou, C., Takahashi, K., Vera, C., 2020. Climate impacts of the El NiñoSouthern Oscillation on South America. *Nature Reviews Earth & Environment* 1, 215–231. <https://doi.org/10.1038/s43017-020-0040-3>
- Campitelli, E., Diaz, L., Vera, C., 2021. Assessment of zonally symmetric and asymmetric components of the Southern Annular Mode using a novel approach. *Climate Dynamics* (under review).
- Hartmann, D.L., Garcia, R.R., 1979. A Mechanistic Model of Ozone Transport by Planetary Waves in the Stratosphere. *Journal of the Atmospheric Sciences* 36, 350–364. [https://doi.org/10.1175/1520-0469\(1979\)036%3C0350:AMMOOT%3E2.0.CO;2](https://doi.org/10.1175/1520-0469(1979)036%3C0350:AMMOOT%3E2.0.CO;2)
- Hersbach, H., Bell, B., Berrisford, P., Biavati, G., Horányi, A., Muñoz Sabater, J., Nicolas, J., Peubey, C., Radu, R., Rozum, I., Schepers, D., Simmons, A., Soci, C., Dee, D., Thépaut, J.-N., 2019. ERA5 monthly averaged data on pressure levels from 1979 to present. Copernicus Climate Change Service (C3S) Climate Data Store (CDS) (Accessed on <19-02-2021>). <https://doi.org/10.24381/cds.6860a573>
- Horel, J.D., 1984. Complex Principal Component Analysis: Theory and Examples. *Journal of Applied Meteorology and Climatology* 23, 1660–1673. [https://doi.org/10.1175/1520-0450\(1984\)023%3C1660:CPCATA%3E2.0.CO;2](https://doi.org/10.1175/1520-0450(1984)023%3C1660:CPCATA%3E2.0.CO;2)
- Irving, D., Simmonds, I., 2016. A New Method for Identifying the PacificSouth American Pattern and Its Influence on Regional Climate Variability. *Journal of Climate* 29, 6109–6125. <https://doi.org/10.1175/JCLI-D-15-0843.1>
- Mo, K.C., Paegle, J.N., 2001. The PacificSouth American modes and their downstream effects. *International Journal of Climatology* 21, 1211–1229. <https://doi.org/10.1002/joc.685>
- Rood, R.B., Douglass, A.R., 1985. Interpretation of ozone temperature correlations: 1. Theory. *Journal of Geophysical Research: Atmospheres* 90, 5733–5743. <https://doi.org/10.1029/JD090iD03p05733>
- Smith, A.K., 1995. Numerical simulation of global variations of temperature, ozone, and trace species in the stratosphere. *Journal of Geophysical Research: Atmospheres* 100, 1253–1269. <https://doi.org/10.1029/94JD02395>
- Wirth, V., 1993. Quasi-stationary planetary waves in total ozone and their correlation with lower stratospheric temperature. *Journal of Geophysical Research: Atmospheres* 98, 8873–8882. <https://doi.org/10.1029/92JD02820>